MARY KAY O'CONNOR PROCESS SAFETY CENTER
TEXAS A&M ENGINEERING EXPERIMENT STATION

21st Annual International Symposium
October 23-25, 2018 | College Station, Texas

Experimental and Computational Study of the Dispersion and Combustion of Wheat Starch and Carbon-Black Particles During the Standard 20L Sphere Test

José Serrano*, Paula Pico, Mariangel Ami, Andrés Pinilla, David Torrado, Carlos Murillo,
Felipe Muñoz, Olivier Dufaud, Nathalie Bardin-Monnier
Department of Chemical Engineering, Universidad de los Andes
Carrera 1 # 18a-12 Bogota, Colombi
Laboratorie Réactions et Génie des Procédés, Université de Lorrain
UMR 7274, Nancy, France
(571) 339-4949 Ext. 1841.
*Presenter: Email: jdj.serrano10@uniandes.edu.co

Keywords*:* CFD, 20L Sphere, Flammable Dust, Starch, Pyrolysis, Combustion.

Abstract

The 20L sphere is one of the standard devices accepted as an international normativity used for dust explosivity characterization. One concern about the effectiveness and reliability of this test is related to the particle size variation due to particles agglomeration and de-agglomeration. These phenomena are determined by the turbulent regime of the dust cloud during the dispersion. This variable must be considered since it determines the uncertainty level of the ignitability and severity parameters of dust combustion. In this context, this study describes the influence of the cloud turbulence on the dust segregation and fragmentation through an experimental and computational study. The behavior of the gas-solid mixture evidenced with the standard rebound nozzle was compared with that observed with six new nozzle geometries. Thereafter, the variations of the Particle Size Distribution (PSD) that occur during the dispersion within the 20L sphere were analyzed for two different powders: carbon-black and micrometric wheat starch. This description is performed with the implementation of two complementary approaches. On the one hand, an experimental approach characterizes the turbulence levels with Particle Image Velocimetry (PIV) tests that are complemented by the description of the PSD variations with granulometric analyses. On the other hand, a computational approach described the dispersion process with CFD-DEM simulations developed in STAR-CCM+ v11.04.010. The simulation results established that the homogeneity assumption is not satisfied with the nozzles compared in this study. Nonetheless, the particles segregation levels can be reduced using nozzles that generate a better dust distribution in the gas-solid injections. Subsequently, an additional first-approach CFD model was established to study the behavior of the combustion step when a starch/air mixture. This model considers the gas-

phase reactions of the combustible gases that are produced from the devolatilization of Wheat starch (CO, CH4, C2H4, C2H6, C2H2 and H2) and allowed to establish the approximate fraction of the particle mass that devolatilizes, as well as to confirm that the modelling of the pyrolysis stage is essential for the correct prediction of the maximum rate of pressure rise.

Nomenclature

CFD – Computational Fluid Dynamics
RANS – Reynolds-Averaged Navier-Stokes
LES – Large Eddy Simulation
IDDES – Improved Delayed Detached Eddy Simulation
DEM – Discrete Element Method
TKE – Turbulent Kinetic Energy
t_v - Ignition Delay Time
$\mathrm{N_i}$ – Nozzle i
P_{max} – Maximum average pressure
$\left(\frac{dP}{dt}\right)_{max}$ – Maximum rate of pressure rise
K_{st} – Deflagration index
V – Volume of the testing vessel
m_p – Mass particle
v_p – Particle velocity vector
F_s – Particle surface forces
F_b – Particle body forces
I_p – Particle moment of inertia
ω_p – Particle angular velocity vector
M_b – Particle drag torque
M_c – Particle total moment from contact forces
CFL – Courant–Friedrichs–Lewy number
Δt – Simulation time-step
u – Maximum flow velocity
Δx – Minimum cell size
V_{rms} – Root-mean-square velocity
V_{rms}^0 – Initial Root-mean-square velocity
t – Testing time
t_0 – Initial testing time
n – Fitting parameter
$v_i{}'$ – Velocity fluctuation of particle i at a given direction
v_i – Velocity of particle i at a given direction
$\bar{v}$ – Average velocity
N – Number of particles present in the sample
ω – Vorticity vector
v – Velocity vector
ρ – Fluid density
ν – Fluid kinematic viscosity
P – Local pressure

1. INTRODUCCTION

1.1. General context and background

In the past few years, the use of dusts, particularly flammable dusts, has become more prominent in certain chemical industries, such as food production, pharmaceuticals, chemical manufacturing, wood processing, and even Oil & Gas industries [1]. Dusts are present in a great variety of processes stablished by these industries such as the transport of materials on rotatory-screw conveyors, milling, grinding, shredding, pulverization, storage, polishing, filtering, among others [2]-[3]. However, dust explosions represent a hazard to these industries in terms of considerable financial losses, damage to physical facilities and often serious injuries to personnel or even fatalities [4], [5].

The first known reported and comprehensive study on the matter was the analysis performed by Count Morozzo of an explosion of flour inside a warehouse in Turin, in the year 1795 [6]–[8]. Fast forwarding to more recent examples, a study of the US Chemical Safety and Hazard Investigation Board (CSB) concluded that, between 1980 and 2005, a total of 281 major dust explosion accidents occurred, resulting in the death of 119 workers, the injury of 718, and the destruction of entire industrial facilities [1], [9], [10]. Similarly, between 1979-1989, The United Kingdom Health and Safety Executive reported 303 incidents; between 1965-1985, The Federal Republic of Germany reported 426 incidents [7] and currently The Chemical Safety Board of the United States reported 50 incidents between 2008-2012 [11]. As a result of the high number of accidents/incidents regarding the use of particulate materials, several efforts have been made to propose, characterize and improve the active and passive security systems of the equipment and the overall process [3].

One of these efforts is related to the correct characterization of the most commonly used dusts in chemical process plants in terms of its explosivity characteristics. These characteristics can be divided in two main categories. The first one aims at determining how likely a certain dust is to explode and can be estimated through the calculation of the Minimum Explosible Concentration (MEC), the Minimum Ignition Energy (MIE), the Limiting Oxygen Concentration (LOC), the Minimum Auto-ignition Temperature (AIT), among others. The second category stablishes the severity level of a potential explosion with the maximum explosion pressure ($\mathrm{P_{max}}$) and the maximum rate of pressure rise ($[\mathrm{dP/dt}]_{\mathrm{max}}$) [1], [12],[13].

The parameters mentioned above can be measured by several standard tests that are based on the dispersion of a known dust mass with air at different operating conditions. Some of the most widely used tests are the 20L Sphere (ASTM E2019-03, ASTM E2931-13 and ASTM E1515-14) [14]–[17] , the Hartmann Tube (ASTM E2019-03) [15] , the BAM Oven, and the Godbert-Greenwald furnace (ASTM E1491-06) [18] . In spite of the fact that the 20L Sphere is currently recognized internationally as a valid and rigorous testing equipment to determine explosivity parameters, recent theoretical, experimental and computational studies have regarded some of its assumptions as highly questionable [1], [7], [12], [19]–[27]. In particular, these studies have agreed that certain operating parameters, such as the geometry of the disperser, the agglomeration and/or de-agglomeration of the dust particles throughout the test, as well as the levels of turbulence have a high influence in the homogeneity of the dust cloud in the dispersion and combustion step, and therefore, could lead to the mis-estimation of the design parameters of the security systems [1], [7], [26], [27], [12], [19]–[25].

1.2. Theoretical Framework: 20L Sphere Standard Test (particle dispersion and combustion)

The 20L standard test was originally designed by Siwek in 1988 to characterize some explosivity parameters of combustible dusts and gases, and became the standard device after replacing the 1 m^3 tube, given that it requires a dust sample with 50 times lower mass [24]. The main parts and components of the geometry are shown in **Fig. 1**.

This geometry can be divided in two main parts. The first part consists of a stainless-steel spherical chamber that occupies a total volume of 20L. This chamber is covered by a cooling jacket system specially designed to dissipate the excess heat produced by the combustion reactions. The interior of the 20L chamber contains an ignition system with two pyrotechnic ignitors that are located at the center of the sphere and that provide an energy spark of 5kJ each. The second part consists of a 0.6L reservoir or canister (where the dust particles are initially stored), a quick action valve and a nozzle that works as a connection between this dust reservoir and the spherical chamber.

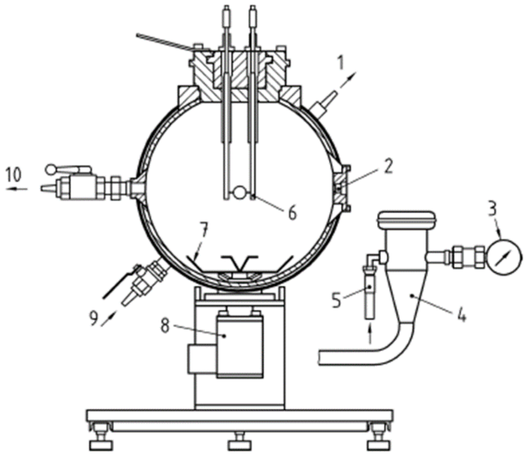

Fig. 1. 20L explosion sphere. **1.** Water Outlet **2.** Pressure sensors **3.** Manometer **4.** Canister (injection chamber) **5.** Air inlet **6.** Igniters **7.** Dispersing nozzle **8.** Quick-action valve **9.** Water inlet **10.** Product outlet [14].

The standard experimental procedure initiates with the de-pressuring of the dispersion chamber (sphere) to a set value of 0.4 bar and the addition of a weighted sample of the studied dust into the canister. Following these activities, the pressure of the canister is increased to a value of 20 bar by allowing the entrance of the dispersion gas, which is usually air unless limiting oxygen tests are performed, in which case its composition can be altered. The next step of the test consist of opening the quick-action valve to let the dust particles pass through the nozzle openings into the 20L sphere by the action of the pressure gradient [28]. Finally, after a given amount of time, the two ignitors have an energy discharge and the combustion process initiates. This time is known as Ignition Delay Time (tv) and is one of the most relevant operating parameters in the development of the test. The determination of an appropriate tv is highly crucial given that this parameter has a noteworthy influence on the turbulence levels reached within the reaction chamber and on the kinetic behavior of the pyrolysis/oxidation reactions. However, several studies on the matter have concluded that an appropriate tv would be approximately 60 ± 5 ms given that, at this point of the process, the concentration of dust particles is somehow homogeneous and the degree of turbulence is high [28].

During the entire process, the mean pressure of the dispersion chamber is increasing at a high rate given the effects of the gas entering the system and the over-pressure wave generated by the combustion reactions. The measurement of these two parameters is the basis for the definition of the deflagration index or $\mathrm{K_{st}}$. This parameter is used to classify dusts materials according to their potential risk of explosion regardless of the volume of the vessel where the test was carried out. **Eq. (1)** shows the mathematical definition of deflagration index [14].

$$K_{st} = \left(\frac{dP}{dt}\right)_{max} * V^{1/3} \qquad \text{Eq. (1)}$$

Table 1 shows the risk level classification according to standard values of K_{st}.

Table 1. Risk level ranges from deflagration index

Risk Level	**K_{st} (bar*m/s)**	**Severity**
St 0	0	None
St 1	0-200	Weak
St 2	**200-300**	**Strong**
St 3	**>300**	**Very Strong**

Most authors agree that the procedure described previously for characterizing dust materials through the standard 20L sphere test can be divided in two main stages: (i) Particle dispersion and (ii) Combustion. For organic particles, the second main stage can be further divided in three main sub-stages: particle heating, particle devolatilization (pyrolysis) and gas oxidation [3], [29]. Some authors have stated that particles of an average diameter lower than 30μm would undergo heating and pyrolysis processes at a sufficiently rapid rate to consider these sub-stages as negligible. However, other authors have demonstrated that, depending on factors such as particle internal and external heat transfer, particle diameter, and the pyrolysis reactions themselves, the pyrolysis sub-step of the process could be the rate-controlling process and should not be discarded [9], [30]. The general reaction pathway for pyrolysis is shown in **Eq. (2)**-**Eq. (3)** [30].

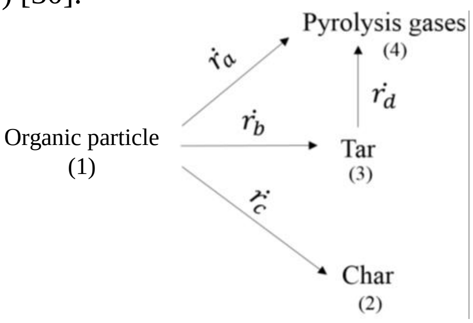

Eq. (2)

$$k_j = A_j \exp(E_j/RT) \qquad \text{Eq. (3)}$$

1.3. State of the art

One of the most important contributions to the improvement of the 20L sphere standard test was developed by Dahoe in 2001, when he discovered that the turbulence levels reached inside the dispersion/combustion chamber are influenced by the Ignition Delay Time, and that these levels also differ from those found inside the 1 m^3 tank at the same dispersion time [24]. From these findings, other authors started questioning how the difference in turbulence levels could affect the results of the test. In particular, Van der Wel showed that the values of the deflagration index measured with the 20L sphere differed significantly with those measured with the 1 m^3 tank for the same dust sample [31]. He attributed this inconsistency to the difference of the turbulence fields that occur in the two geometries.

Other studies have focused their attention on the evaluation of the influence of the nozzle type on the turbulence levels reached and the concentration homogeneity. These authors include Murillo [28], Dahoe [24] and Mercer [7], who separately analyzed different nozzle geometries and concluded that this factor is indeed one of the parameters that could be modified in order to obtain higher levels of homogeneity and therefore, more accurate and reliable test results.

As for other parameters, such as the particle size distribution, the studies made by Callè [32], Cashdollar [33] and Soundararajan [34] have led to conclude that, in the micrometric range, the reduction of the particle size tends to have a positive effect on the explosion severity, particularly on the maximum pressure reached. On the other hand, in the nanometric scale, this trend is not maintained as the reduction of the particle size only influences the MIT and MIE [35].

Besides the experimental studies mentioned above, there have been some efforts to use certain computational tools to study the validity and improvement of the standard test. As an example, Di Benedetto [1] used Computational Fluid Dynamics (CFD) to show that the turbulence levels suffer a decay over time and that the ignition points (at the geometrical center of the sphere) have higher turbulence levels than the remaining parts of the domain. Other studies have analyzed the influence of particle properties, nozzle geometry and initial agglomeration shape in the turbulence levels reached [21], [33]. While most of the CFD studies limit their reach to the dispersion stages, Skjold [36], Salamonowicz [37] and Redlinger [38] have used commercial software, such as FLUENT and FLACS, and simplified chemical reaction mechanisms to successfully simulate the combustion stage and obtain some relevant information.

Considering the previous remarks, this study will be focused on applying experimental and computational tools in order to study how the behavior of the discrete phase (particles) during the dispersion stage is influenced by the geometry of the disperser and by the dust material (Wheat starch and Carbon-black), and how this affects the validity of the assumptions of the standard test. Additionally, this study contains an initial attempt at simulating the combustion stage with a detailed kinetic combustion mechanism and at determining the fraction of the particles that devolatilize into the combustion gases.

2. METHODOLOGY

The upcoming section addresses in detail the methodology followed for the experimental and CFD approaches to analyze the dispersion and combustion stages of the 20L Sphere.

2.1. Experimental approach

To evaluate the dispersion stage and the most relevant variables, the 20L Sphere was modified by the installation of visualization windows through the axis center and two piezoelectric transducers on the equatorial plane at the wall of the dispersion chamber to monitor the pressure profile. Moreover, the dust dispersion dynamics and agglomeration phenomena were analyzed experimentally by Particle Image Velocimetry (PIV) and Granulometric analysis techniques using the standard rebound nozzle geometry.

The first technique allows the study of the variation of the velocity field at the center of the 20L Sphere, in a region of $3 \times 3\ cm$, by the determination of the average motion of small groups of particles contained within small regions, known as interrogation spots [39]. In addition, the assembly used includes a high-speed camera Phantom V91 (**Table 2**) placed in front of a visualization window, a laser focus at the center of the sphere to illuminate the particles and the MATLAB ® tool, PIVLab® to process the images captured. Furthermore, the measures of Carbon-black were performed neglecting additional light sources, as the black body optical properties of this dust.

Table 2. Phantom V91 technical specifications

Specifications	Value
Resolution	$480 \times 480\ px$
Exposure	$150\ \mu s$
Area	$(2.95 \times 2.80)\ cm$
Framerate	$6410\ fps$
Time interval	$156\ \mu s$

The Granulometric Analysis was used for the measurement of the variation of the PSD using a laser diffraction method to study the de-agglomeration/agglomeration phenomena. The equipment handled was a HELOS-VARIO/KR (Sympatec) with an optic system composed by a laser emission and detection device. For the measurements, the dispersion chamber was located between the sensor and the detection unit.

Furthermore, the dust materials used in this research are the micrometric Wheat starch and Carbon-black, because of the widely industrial use, the extensive dust dispersion studies, and the well know explosibility parameters [27], [40]. One of the more important variables which characterizes the dust materials is the particle size distribution in a cumulative distribution function, as shows the **Fig. 2**.

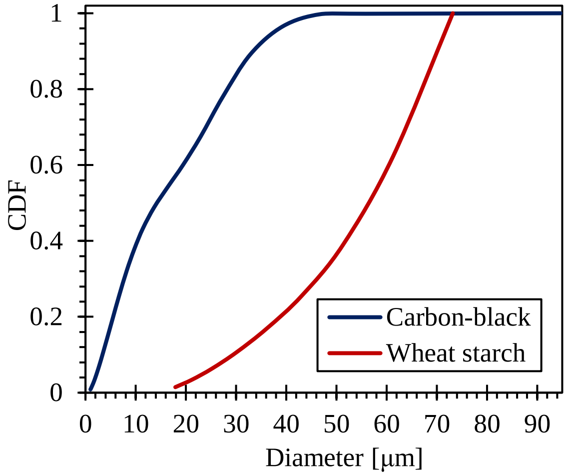

Fig. 2. Average particle size distribution (PSD) of the Carbon-black and Wheat starch dust samples

On the other hand, microscopy technique was used to study the agglomerate shapes of the dust materials. **Fig. 3** shows the most common configurations of Wheat starch, which were adjusted to easier shapes; like triangular, cube and line assemblies. Moreover, the most common agglomeration shape of the Carbon-black was a line configuration, comparable to **Fig. 3c.**

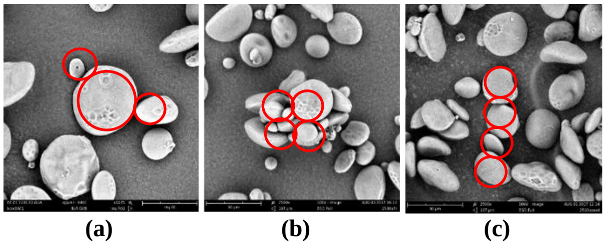

Fig. 3 Most common agglomerate shapes in Wheat starch samples **(a)** Triangular **(b)** Cube **(c)** Line

2.2. CFD modelling

Given that this study is focused on both, the dispersion and combustion stages of the standard test, two separate CFD sets of simulations were established with the aim of testing different variables and performing various analyses.

The dispersion stages were studied through two different dust materials and seven disperser geometries. The two selected materials were micrometric Wheat-starch and Carbon-black. The seven dispersers included the standard nozzle, a symmetric nozzle proposed by Murillo [28] and five nozzles proposed by this study. **Fig. 4** contains a schematic representation of these nozzles.

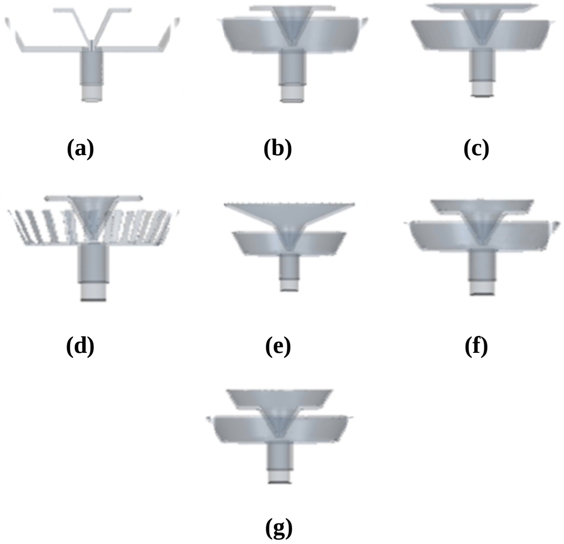

Fig. 4. Disperser geometries used. **(a)** Standard (N1). **(b)** Symmetric (N2). **(c)** N3. **(d)** N4. **(e)** N5. **(f)** N6. **(g)** N7.

As will be meticulously explained in the following sub-sections, the physical model selected to simulate the dispersed phase (DEM) requires the establishment of an initial shape for the particle agglomerations. Considering the microscope images of Wheat starch shown in **Fig. 3**, three initial shapes were selected: line, cube and triangle (see **Fig. 5**).

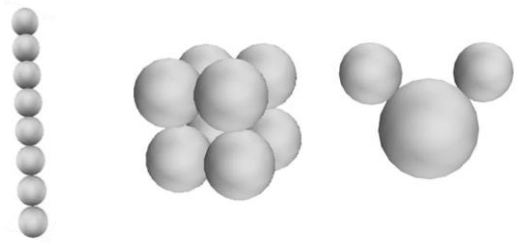

Fig. 5. Initial agglomeration shapes considered for the dispersion simulations. **(a)** Line. **(b)** Cube. **(c)** Triangle

Considering that it is highly desirable to find the combined effect of these variables, the simulations of Wheat starch were run with each of three initial agglomeration shapes and the standard and symmetric nozzles. In contrast, the simulations for Carbon-black were run with the line shape and the seven nozzles.

The CFD model constructed for the combustion stage considered only the standard disperser and used only the pyrolysis gases of Wheat starch. The use of this method was performed as a first approximation and simplification of the complex process of organic particles combustion [41]. In addition, the generation of tar and char, described in Section 1.2, is neglected because of the significant increase of the gas formation rates and the considering of complete devolatilization at high temperatures, as upstream of the flame [29], [41].

Furthermore, the pyrolysis gases mixture composition of Wheat starch sample was established from an adjustment of the study of flash pyrolysis reactor by Bozier [42], taking into account the variation of compositions at different reactor temperatures and the typical flame temperature of this dust combustion [29]. The gas mixture compounds loaded on CFD simulations were $H_2, CH_4, CO, C_2H_4, C_2H_6$, C_2H_2[42].

Additionally, taking into consideration the PSD of Wheat starch (**Fig. 2**) was on average greater than $30\,\mu m$, therefore the devolatilization would become a rate-controlling step of combustion process [29]. Consequently, this study proposes the study of this restriction using a proportional constant (k_c), which correlates the equivalent ratio between the solid mass of the organic dust (m_o) and the mass of pyrolyzed gases (m_p), as shown in **Eq. (4)**. This simplification was made considering the complexity of measuring and lack of data about the pyrolysis kinetics of Wheat starch at conditions of 20L Sphere standard test.

$$\frac{m_p}{m_o} = k_c \qquad \text{Eq. (4)}$$

Moreover, the value of k_c can be interpreted as the percentage of solid mass converted to pyrolyzed gases, which according to the work done by Zhang, et al. [43], this variable could value 0.86 for corn starch, which is comparable with Wheat starch used in this study. However, the conditions at the 20L Sphere standard test could affect the prediction of k_c [43] and the state of the sample at measurement. For that reason, this study evaluated the combustion of a pyrolyzed gas mixture at different k_c (taking the value reported by Zhang, et al. [43] as the middle point, the upper bound of the variable and a proportional lower bound), of a mass of 10 g of Wheat starch, which correspond to a fuel-equivalence ratio $(F/A) = 1$ [29], as shown the **Table 3**. Furthermore, there were made several test to validate the behavior of the combustion dynamics at the most relevant value of k_c and different (F/A), in order to compare with the experimental data found by Dufaud, et al.[29].

Table 3. Simulated cases to evaluation of k_c at combustion of pyrolyzed gases

Cases	(F/A)	k_c
1	1	1.00
2	1	0.86
3	1	0.60

On the other hand, the kinetics parameters of the combustion reactions were taken from the optimized mechanism of methane-air combustion based on GRI-Mech 3.0 with 30 species [44]. This mechanism was selected because it involves all the pyrolysis gases of the Wheat starch and the contrast of the combustion behavior prediction between the complete mechanism of 53 species, don't present a significant difference [44].

2.1.1. Spatial discretization

The discretization of the geometry was made by the finite-volume method. A polyhedral mesh was selected due to the generation of more neighboring cells and optimal directions for the flow when compared to other models, such as tetrahedral [20], [45].Additionally, previous CFD studies used the polyhedral mesh for different applications and obtained good agreement with experimental data [20], [27], [46]. Moreover, the surface remesher was used for the re-triangulation of the surface to allow cell refinement over certain volume regions [45], in order to model accurately the fluid behavior in the most complex zones (nozzle and ignitors) of the geometry and avoiding divergence, as shown in **Fig. 6**.

Furthermore, the prism layer model was added because of the important source of vorticity at the walls of the geometry, in order to improve the prediction of the flow and turbulence across the boundary layer [45]. The resultant mesh was around 820,000 cells with an average cell quality of 0.738.

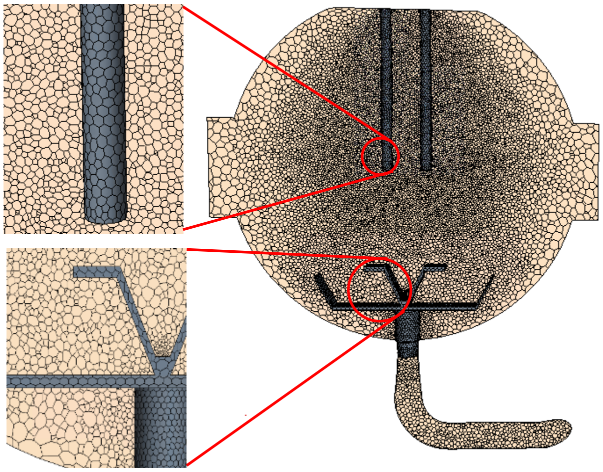

Fig. 6. Mesh of the 20L Sphere and refinements on the ignitors and nozzle near zones.

2.1.2. Boundary and initial conditions

The initial and boundary conditions loaded on the simulations were in agreement with the experimental settings and the international standard ASTM E1226 [14], however the cooling jacket was simulated as a thermal boundary at constant temperature, as shown in **Table 4**.

Table 4. Initial and boundary conditions

Condition	Value
Initial pressure [bar]	20 (Canister), 0.4 (Sphere)
Initial temperature [K]	300
Boundary solid type	No-slip wall
Thermal boundary [K]	Adiabatic (Canister), 300 (Sphere)

2.1.3. Physical models' selection

The physical models that describe the overall system of the 20L Sphere were selected considering the accuracy and suitability of the model for this application, as well as computational power and time requirements.

Considering that the dispersion stage of the process is a phenomenon of a two-phase nature, a Eulerian-Lagrangian problem formulation was selected as the general approach. Broadly speaking, the Eulerian representation of a fluid flow considers the fluid properties (such as velocity, pressure, and density) as field functions of time and position within a specific control volume, which makes this approach very suitable to model 'continuous' flow phases, such as the gas phase present in the 20L Sphere. On the other hand, the Lagrangian approach is focused on describing and tracking the motion of each individual particle in order to determine the fluid flow properties. The consideration of each particle as an individual entity indicates that the Lagrangian model is highly appropriate to describe the combustible dust particles of this study [47], [48].

The upcoming paragraphs contain the specificities of the approaches followed for the Eulerian (gas) and Lagrangian (dust particle) phases.

(i) Gas-phase modelling: The fundamental constitutive equations of a continuous flow were resolved through the the Reynolds-Averaged Navier-Stokes (RANS) approximation, coupled with the standard k-ϵ turbulence model to calculate the Reynolds-stress tensor. In spite of the fact that previous studies on the matter of the 20L Sphere have mainly used a combined LES-RANS (IDDES) approach with a k-ω SST turbulence model [20], [27], [49], [50], as will be seen in the forthcoming section, at the later stages of the dispersion step, the fluid domain can be considered isotropic, which makes the flow appropriate to be described by RANS [51]. Additionally, it can be stated that the k-ϵ turbulence model is very well-fitted for high Reynolds applications, provides a good balance between accuracy and computational time and has been successfully used for CFD modelling of the combustion stages in the context of the 20L Sphere standard test [36], [37]. The k-ϵ turbulence model was configured with an upwind second-order convection scheme

(ii) Particle modelling: The behavior of this phase was modelled through the Discrete Element Method (DEM), an extension of general Lagrangian approach. As opposed to the general model, DEM tracks the motion of the entire set of particles contained within the system, and is able to account for the interactions between particles [45]. These characteristics of DEM are particularly useful for this application given that one of the main objectives of this study is to analyze the process of particle agglomeration/de-agglomeration during the dispersion stage, which is a phenomenon highly influenced by particle-particle interaction forces. Several studies have previously used DEM to model different particulate materials inside closed systems with very accurate results [52], [53].

The general equations of motion of the particles are derived from the classical mechanics' equation of conservation of linear and angular momentum (**Eq. (5)-Eq. (6)**) [45].

$$m_p \frac{d\boldsymbol{v_p}}{dt} = \boldsymbol{F_s} + \boldsymbol{F_b} \qquad \text{Eq. (5)}$$

$$\boldsymbol{I}_p \frac{d\boldsymbol{\omega_p}}{dt} = \boldsymbol{M_b} + \boldsymbol{M_c} \qquad \text{Eq. (6)}$$

The term of the surface forces represents the overall momentum transfer from the gas (continuous phase) to the particles. This force term was considered as the sum of the contributions of the drag force and the pressure gradient force. The drag coefficient was estimated through the Schiller-Nauman correlation given that the agglomerates were assumed to be comprised of completely spherical particles.

On the other hand, the body forces were assumed to be the sum of the gravity forces and the interparticle contact forces. These contact forces were calculated through the Hertz-Mindlin no-slip contact model, which is a variation of the standard non-linear spring-dashpot model [54]

As for the combustion step of the standard test, the transport equations related to each one of the chemical species involved were resolved through the Complex Chemistry transport model. This model is well-fitted for this particular application given that it is a highly rigorous approach that integrates all the source terms of the transport equations over time and considers that the reactions are limited by their actual kinetics and not by the rate in which the species and heat are mixed into the flame zone by the turbulence [45]. The solver selected for the time integration of the source terms was CVODE.

Additional to the models mentioned previously, it is relevant to highlight that both main stages of the standard test (dispersion and combustion) are unsteady phenomena. Taking this into account, an Implicit Unsteady method, coupled with a second order discretization scheme, was selected. The time-step was set for all simulation aiming for a Courant number of 1 as this ensures that the flow travels only one cell each time-step.

$$CFL = \frac{u\, \Delta t}{\Delta x} \qquad \text{Eq. (7)}$$

3. RESULTS AND DISCUSSION

This section contains the main results of this study and a detailed discussion of the implications of the data acquired through experimental and CFD means. These results are divided in two main sub-sections: (i) Analysis of the dispersion stage of wheat starch and Carbon-black, and (ii) First approach to the modelling of the combustion stage of the 20L standard test.

3.1. Evaluation of the effect of turbulence on the agglomeration/de-agglomeration of the particles and the overall dispersion step of the test

As it was mentioned previously, this sub-section has the main objective of evaluating certain phenomena that occur during the dispersion stage and how these could potentially affect the subsequent pyrolysis/combustion stage, which affects the reliability of the assumptions of the standard test.

3.1.1. CFD validation and effect of the disperser on the pressure profile

The validation of the CFD model stablished for this part of the analysis was performed through the comparison of the average pressure profile of the sphere region obtained by CFD and the pressure obtained experimentally by two transducers located at the equatorial plane of the sphere. This variable was selected for validation purposes over temperature or particle velocity as the maximum pressure and maximum rate of pressure rise are the fundamental variables that determine the explosive potential of a certain dust material [36]. **Fig. 7** contains the experimental and CFD pressure profiles for the three initial particle shapes of Wheat Starch and the seven nozzles for Carbon-black.

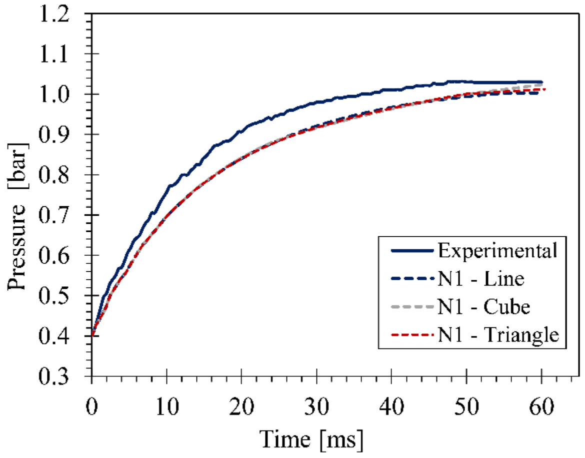

(a)

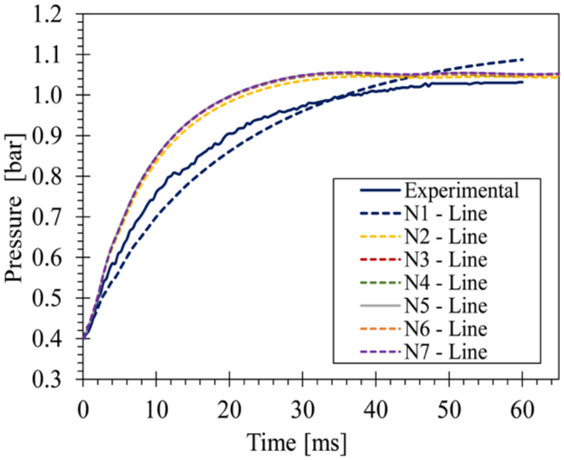

(b)

Fig. 7. Comparison of the sphere pressure profile obtained experimentally and by CFD for **(a)** Wheat starch and **(b)** Carbon-black

From **Fig. 7** it can first be stated that both, the experimental and CFD results are congruent with previous experimental and theoretical studies as the sphere undergoes a very rapid pressure increase up to 20ms, followed by a more gradual increase until the system reaches the desirable pressure of 1 bar at approximately 60ms (standard Ignition Delay Time) [28], [55]. This can be explained by the fact that, at the very beginning of the test, the pressure gradient between the sphere and the canister is high, which directly translates into a high driving force that induces a high rate of mass, momentum, and energy transfer. As the pressure of the sphere increases (and the pressure of the canister decreases), the driving force is lowered and therefore, the rate of pressure rise within the sphere also decreases.

Fig. 7 also suggests that the CFD model constructed for both materials provides a very accurate prediction of the sphere pressure given that the deviations from the experimental points (for the standard nozzle) do not overcome 8.6% for Wheat Starch and 5.5% for Carbon-black (with an average error of around 5.03% for Wheat Starch and 3.76% for Carbon-black). To better highlight the quality of the prediction achieved, the experimentally-measured pressure values were plotted against their CFD counterparts to obtain **Fig. 8**. It is important to mention that **Fig. 8** only contains the pressure values obtained every 0.5ms in order to have the same number of experimental and CFD points (the low time-step selected for the simulations results in a significantly higher number of CFD points). However, it should be noted that the intermediate values have the same tendency and deviation and that 0.5ms intervals can correctly represent the entire data set.

Fig. 8 shows that the CFD model tends to under-predict the pressure values for both materials. This behavior is consistent with previous CFD studies [20] and can mainly be explained by the selected physical models of agglomeration/de-agglomeration and the set-up parameters (such as Poisson’s ratio, Young’s modulus, Tensile strength, among others) used for Wheat starch and carbon-black. Additionally, from **Fig. 7** and **Fig. 8** it can be noted that the highest errors are found at intermediate times (from around 10ms to 40ms), which would suggest that the assumptions of the CFD model (refer to section 2.2) are more appropriate for very high and/or very low velocities and turbulence levels (beginning of the test and end of the dispersion stage, respectively).

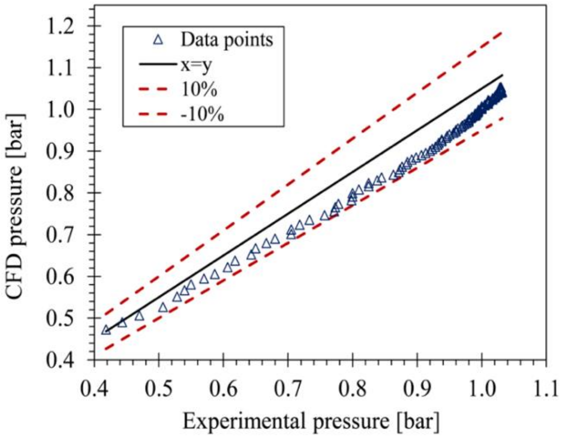

(a)

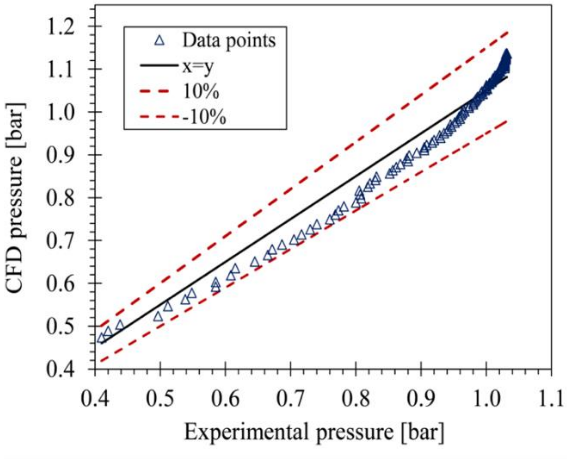

(b)

Fig. 8. Pressure profile obtained experimentally vs. CFD with the standard dispersion nozzle. **(a)** Wheat Starch and **(b)** Carbon-black

On the other hand, **Fig. 7(a)** implies that the initial agglomeration shape does not have a considerable influence on the behavior of the sphere pressure with time. This result is interesting given that, as will be thoroughly analyzed in the upcoming sub-sections, the initial shape of the particles is very much an influential parameter on the degree of de-agglomeration reached at the end of the dispersion stage and on the validity of the assumption that the particle concentration is homogeneous throughout the domain of the sphere.

To finalize this sub-section, it is relevant to highlight that the pressure profile obtained for the standard nozzle differs from the one obtained with the remaining six nozzles (**Fig. 8(b)**). As can be expected, this behavior is attributed to the geometrical differences between the nozzles and the turbulence levels reached in each case. **Fig. 9** shows the average CFD Turbulent Kinetic Energy (TKE) for Carbon-black. As can be seen in **Fig. 9**, a significantly lower TKE peak is obtained with the standard nozzle, which influences directly the average sphere pressure and explains the pressure behavior found in **Fig. 7(b)**.

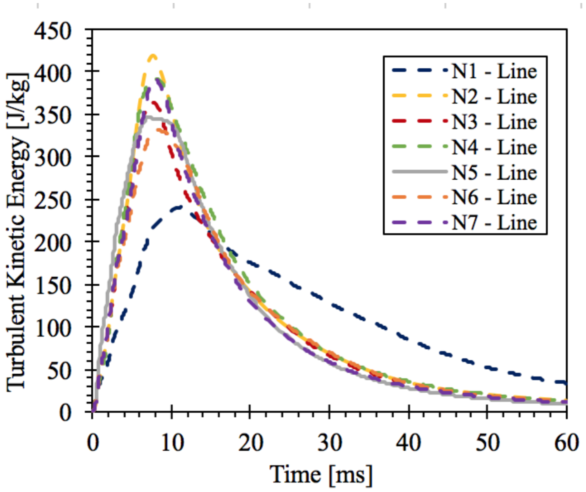

Fig. 9. Average CFD Turbulent Kinetic Energy profile for Carbon-black

3.1.2. Analysis of particle velocity at the ignition zone

As it was mentioned on the Methodology section, a PIV analysis was performed at the center of the sphere to obtain the particle velocities at the x and y plane coordinates and compare then with those obtained by CFD. Considering the considerable number of particles present within the system, the two component velocities of each particle were averaged by the total number of particles through the definition of the root-mean-square velocity. **Fig. 10** shows the V_{rms} magnitude obtained experimentally and by each of the CFD simulations.

$$V_{rms} = \sqrt{\frac{1}{N}\sum_{i=1}^{N}\left(v'_{xi}\right)^2 + \frac{1}{N}\sum_{i=1}^{N}\left(v'_{yi}\right)^2} \qquad \text{Eq. (8)}$$

$$v_i{}' = v_i - \bar{v} \qquad \text{Eq. (9)}$$

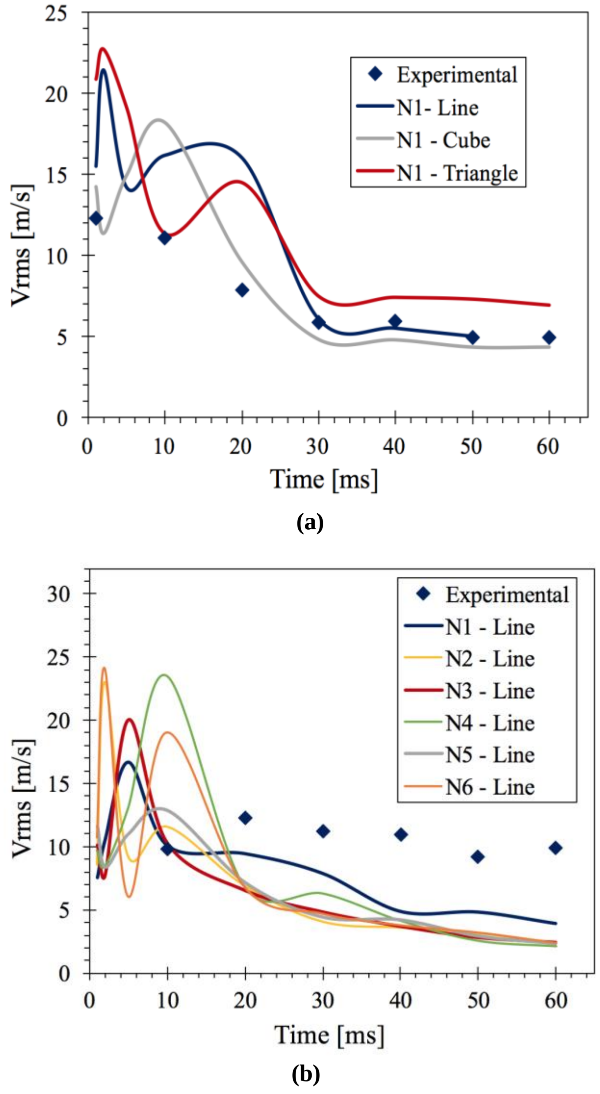

(a)

(b)

Fig. 10. Root-mean-square velocity at the center of the sphere for **(a)** Wheat starch and **(b)** Carbon-black. The experimental measurements were taken with the standard nozzle (N1).

The results shown in **Fig. 10** indicate that the dispersion process can be divided into two main sub-stages. The first one (from 0 to ~30 ms for Wheat-starch and from 0 to ~20 ms for Carbon-black) includes a highly fluctuating particle flow and a high degree of velocity decay that coincides with the high degree of TKE decay of **Fig. 9**. Considering only this sub-stage, it can be stated that the lowest V_{rms} values, as well as the slowest rate of V_{rms} decrease are obtained with the standard nozzle and Carbon-black particles. This result is consistent with both, the TKE and pressure CFD profiles shown previously.

The second sub-stage (from ~30 to ~60ms for Wheat-starch and from ~20 to ~60ms for Carbon-black) shows a much smoother V_{rms} decrease over time and a less prominent difference between the V_{rms} values for the different nozzles, initial agglomeration shape and particle materials. This result is in agreement with previous studies [56], [57] as these state that 60ms is the testing time where the turbulence reaches constant levels over time and the flow becomes approximately isotropic (the three velocity components are equal in magnitude).

As it was suggested by Dahoe et al. [24], [25], the decreasing behavior of the V_{rms} and TKE over time can be explained by the three main mechanisms that induce turbulence in the system. The first mechanism is the baroclinic contribution to the change of vorticity within a velocity field (last term of **Eq. (10)**).

$$\frac{D\boldsymbol{\omega}}{Dt} = (\boldsymbol{\omega}\cdot\boldsymbol{\nabla})\boldsymbol{v} - \boldsymbol{\omega}(\boldsymbol{\nabla}\cdot\boldsymbol{v}) + \nu\boldsymbol{\nabla}^2\boldsymbol{\omega} + \frac{\boldsymbol{\nabla}\rho \times \boldsymbol{\nabla}P}{\rho^2} \qquad \text{Eq. (10)}$$

At the very beginning of the test, the particles are flowing through a cylindrical channel that connects the canister to the sphere. Consequently, the pressure and density gradients are expected not to have the same direction and to have a significant magnitude, producing high vorticity, velocity, and turbulence levels. However, as the particles start entering and dispersing inside the sphere domain, the pressure gradients decrease and the contributions from the baroclinic effects become insignificant [24], [25].

The other two sources are the turbulence that arises from the flow interaction with the wall friction [58] and the shear turbulence. These two remain present all throughout the entirety of the test but their contribution to the turbulence levels is not significant. Subsequently, considering that the baroclinic effect has the highest influence on the turbulence levels reached, the decline on the TKE and velocity can be attributed to the decline on the baroclinic contribution to the vorticity.

On the other hand, the decaying nature of the V_{rms} for Carbon-black shown in **Fig. 10 (b)** was fitted to the inverse power-law equation proposed by Dahoe et al. [24] (Eq. (11)) from 20ms to 120ms. This time range was selected for the fitting given that the equation proposed by Dahoe is mostly used when the rapid decay that follows the TKE peak has already been surpassed. **Table 5** shows the parameter fitted by the application of the standard least square method and the average deviation between the CFD and the fitted V_{rms} values.

$$\left(\frac{V_{rms}}{V_{rms}^{0}}\right) = \left(\frac{t}{t_0}\right)^{n} \qquad \text{Eq. (11)}$$

Table 5. Fitting parameter of the equation proposed by Dahoe et al. [24] for Carbon-black

Nozzle	Parameter n	R^2
N1	-0.8250	0.3783
N2	-0.9338	0.0613
N3	-0.9932	0.0567
N4	-0.9463	0.2365
N5	-1.0244	0.0545
N6	-0.9814	0.0630

The comparison between the magnitudes of the R^2 for each nozzle (**Table 5**) and the V_{rms} values (**Fig. 10 (b))** indicate that the data set predicted by CFD can be fitted very well to the decaying function proposed by Dahoe et al. [24], [25] and, therefore, that the CFD results are in complete agreement to the data of that particular study. In addition, **Table 5** shows that the obtained fitting parameter n does not differ significantly for the six nozzles being studied. This suggests that, from around 20ms to the selected Ignition Delay Time, the rate of decay of the V_{rms} is not strongly influenced by the geometry of the nozzle.

3.1.3. Evaluation of the agglomeration/de-agglomeration process

The agglomeration and de-agglomeration phenomena of dust particles was studied in a quantitative approach by the determination of the mean diameter after dispersion (d_{50ad}), as shown in **Fig. 11**, and bear in mind the mean diameter before dispersion (d_{50bd}), which are 14.5 and 56.5 μm for Carbon-black and Wheat starch respectively.

Fig. 11(a) exhibit a slightly de-agglomeration of the Wheat starch at the center of the sphere along the dispersion, which suggest that the overriding stage is at the beginning of the injection process, with a reduction of 68% of the mean diameter of the particles. This behavior is according to the high-pressure gradients when the particles moves through the canister exit to the nozzle. That assumption is in accordance with Weiler, et al. [59] who found that the disintegration of micron sized agglomerates occurs mainly by shear stress induced by vortices, which are generated by the baroclinic effect near the nozzle area [1]. Moreover, the velocity gradient in this section generates rotary stresses which promote the de-agglomeration, making the connection duct as the overriding region of this phenomena, as well as Kalejiaye, et al [12] found.

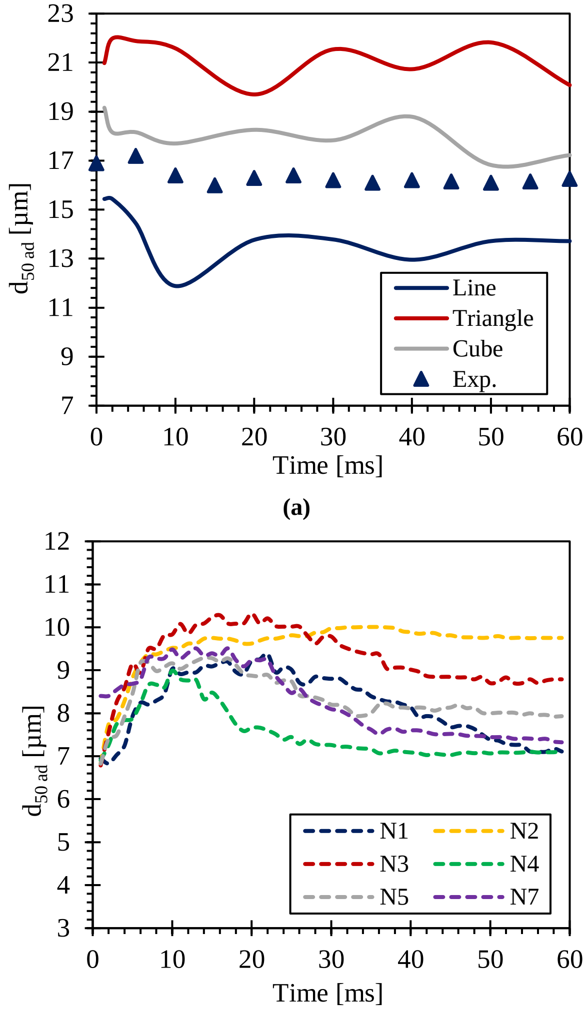

(a)

(b)

Fig. 11 Mean diameter during dispersion of **(a)** Wheat starch and **(b)** Carbon-black particles. The experimental and CFD data of Wheat starch were taken at the center of the sphere with standard nozzle (N1)

Therefore, the line agglomerate shape had a higher de-agglomeration, as shown in **Fig. 11(a)**, since this configuration has more surface area available for turbulent stresses transfer than other configurations. Additionally, the results of the mean diameter of Carbon-black (**Fig. 11(b)**) on the sphere show a de-agglomeration of more than 45% since the beginning of the dispersion process. Nonetheless, the Carbon-black particles have a slightly agglomeration stage until 20 ms. This behavior is in agreement with the smaller particle size which promotes the effects of cohesive forces and the generation of agglomerates during collisions [60].

On the other hand, (**Fig. 11(b)),** indicates that the nozzle variation marginally affects the de-agglomeration of Carbon-black particles, where the nozzles 1 and 4 had the higher values. The previous statement is explained by the lower velocity decay, which hinders the effects of cohesive forces and agglomeration, as found by Sanchirico, et al. [19].

3.1.4. Evaluation of the homogeneity of particle concentration

The evaluation of the homogeneity of the dust cloud is related with the concern about the Minimum Explosive Concentration (MEC). As mentioned earlier, this variable is calculated from the dust nominal concentration, which assumes a homogeneous dispersion of the dust along the sphere. Therefore, the dimensionless concentration **Eq. (12**) is used as a homogeneity degree of the dust cloud.

$$C_{ratio} = \frac{C_{ignition}}{C_{nominal}} \qquad \text{Eq. (12)}$$

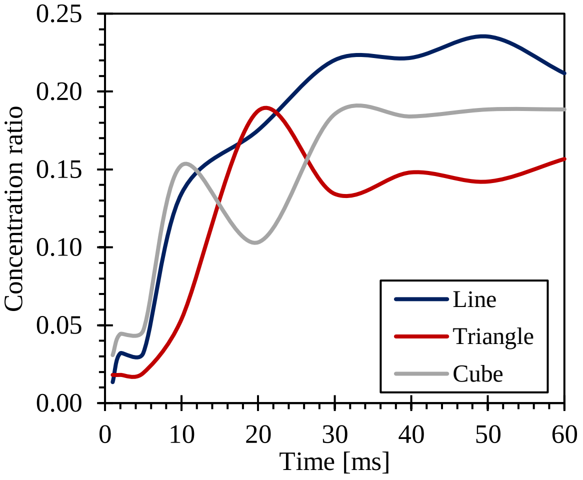

(a)

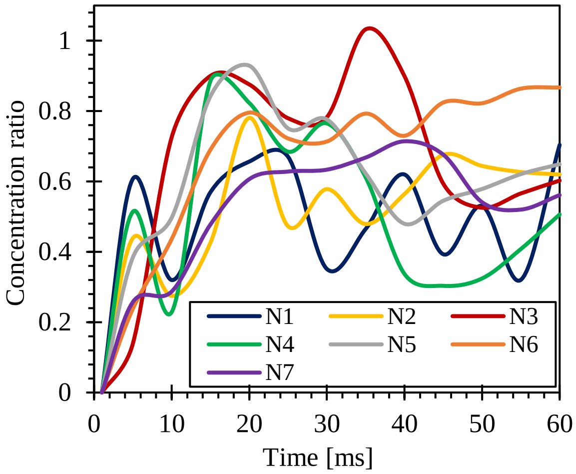

(b)

Fig. 12 Concentration ratio in the ignition zone of **(a)** Wheat starch and **(b)** Carbon-black.

The results shown in **Fig. 12** indicate that the real concentration is lower than the nominal concentration for all the different nozzle and agglomerates at the ignition time. Moreover, the line shape of wheat starch agglomerate exhibits a better homogeneity (**Fig. 12(a)**), and this behavior can be explained by the higher de-agglomeration (**Fig. 11(a)**) that benefits the increase of the dispersibility of the dust.

Additionally, the outlines of the concentration ratio of carbon black for the different nozzle types (**Fig. 12b**) suggest a similar behavior along the dispersion stage, with greater fluctuations at the earlier times ($< 30\ ms$) and no significance difference at the ignition time. Nevertheless, nozzle 6 develops a slightly better homogeneity, followed by nozzle 1.

Furthermore, the results in **Fig. 12** show that the homogeneity of the Carbon-black dust cloud is better than the Wheat starch one. It can be described by the lower particle diameter of carbon black, which decreases the drag force per particle [27] and enhances the displacement of more particles to the center of the sphere, where the velocity fields are lower [28].

3.2. First approach to pyrolysis and fuel combustion

3.2.1. Model validation

Prior to the application of the CFD model established for the combustion stage of the standard test, an initial simulation was run to evaluate the validity of the reactions kinetic model, the thermodynamic data of the species involved and the overall CFD model, as well as analyze the general behavior of the flame and its propagation rate. The validation simulation was run with a gas equivalence ratio of 1.5 and it was compared to the equivalent experimental data taken by Dufaud et al. [29]. **Fig. 13** shows the evolution of the flame front at an Ignition Delay Time of 60 ms.

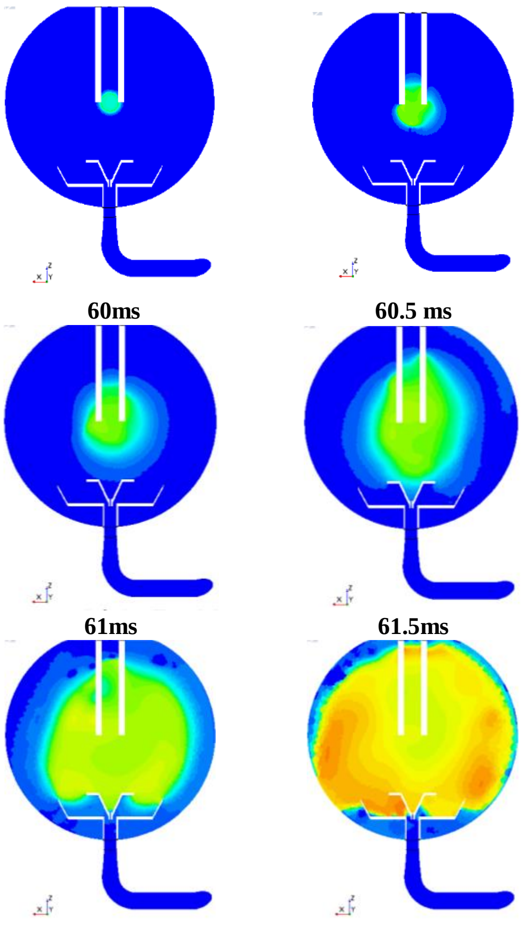

60ms **60.5 ms**

61ms **61.5ms**

62ms **62.5ms**

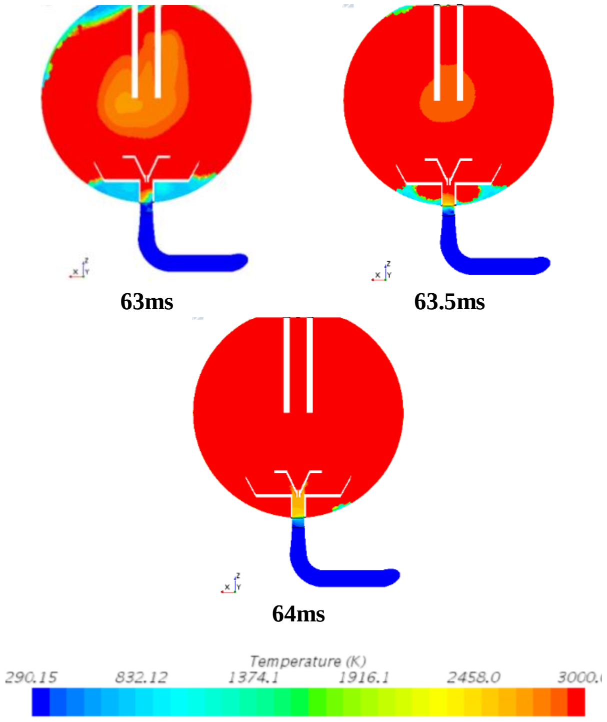
63ms

63.5ms

64ms

Fig. 13. Evolution of the flame front for the validation case

As can be seen in **Fig. 13**, the time passed from the beginning of the reaction to a state of total flame propagation within the system does not exceed the value of 4ms. This indicates that the environment in which the pyrolysis gases are present at 60 ms is highly reactive. Besides the conditions of temperature, pressure and fuel composition, the reaction rates are aided by the levels of turbulence that the system reaches after a dispersion time of 60 ms. From **Fig. 13** it can also be noted that the flame front is not perfectly spherical and, at certain times, has a preferred direction. This can be explained by the fact that the solid ignitors act as obstacles to the general flow and that, despite that at the Ignition Delay Time the system is close to being isotropic (refer to sub-section 3.1.2), there are still certain velocity gradients that direct the flame to a particular direction.

The selected variable to compare the CFD model to the literature experimental value was the maximum rate of pressure rise as this parameter is fundamental to the calculation of the deflagration index. **Table 6** shows the CFD and literature values and the deviation between the two.

Table 6. Comparison between the validation simulation and the data of Dufaud et al. [29]

CFD $\left(\frac{dP}{dt}\right)_{max}$ [bar/s]	**Dufaud et al. $\left(\frac{dP}{dt}\right)_{max}$ [bar/s]**	**%Error**
1721	2050	16%

As can be seen in **Table 6**, the proposed model fits well to the literature data. However, it should be noted that the chemical reaction model selected is highly rigorous and that the combustion reaction path considers several main and secondary equations. Consequently, it can be suggested that the deviation to the literature data is attributed to the calculation of the fuel equivalence ratio and, therefore, the concentrations of each of the initial chemical species. This remark will be further discussed in the following sub-section.

3.2.2 Evaluation of explosibility parameters and k_c to wheat starch combustion

The evaluation of explosibility parameters of Wheat starch at different values of k_c (reported on **Table 3**) were simulated in order to find the better fit with experimental values reported by Dufaud, et al. [29] at a $(F/A) = 1$. The $(dP/dt)_{max}$ was the chosen variable for the comparison because the relevance for the design of safety equipment [38]. Therefore, **Fig. 14** indicates a significantly difference (one order of magnitude) between the CFD and experimental data of the combustion of starch dust, validating the impact and the predominance of the pyrolysis step during a dust explosion [29], [41].

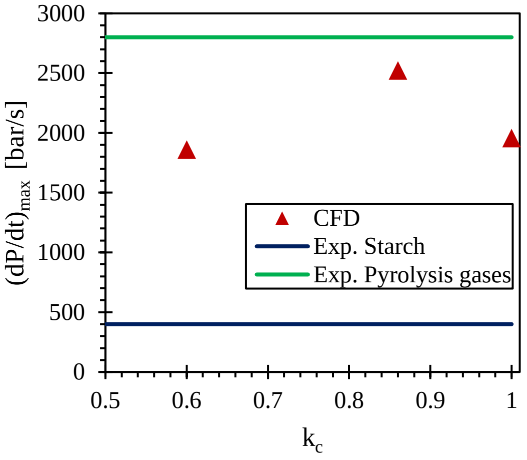

Fig. 14. $(dP/dt)_{max}$ behavior at different values of k_c at (F/A) equal to 1. The experimental data of pyrolysis gases and starch were taken from Dufaud, et al [29].

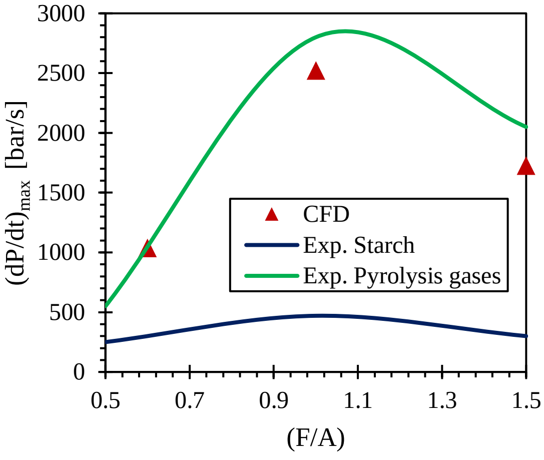

Fig. 15. $(dP/dt)_{max}$ behavior at different values of (F/A) at constant k_c equal to 0.83. The experimental data of pyrolysis gases and starch were taken from Dufaud, et al [29].

Additionally, it could be seen that, when an evaluation of a value lower than 0.3 for k_c, the value of $(dP/dt)_{max}$ simulated would be in the same order of magnitude of the experimental data. Nevertheless, a lower value of the k_c suggest that the combustion of wheat starch generates more tar and char than pyrolysis gases, which is contradictory at conditions of combustion inside the 20L Sphere test [29].

In the other hand, the performance of the CFD results reveals an inaccuracy since the maximum value of $(dP/dt)_{max}$ was reached at $k_c \neq 1$. That indicates that the stoichiometric F(dust)/A had some errors, because a generation of an excess of fuel at this point, as shown **Fig. 14**. Moreover, the results obtained in this study suggest the calculation of stoichiometric concentration of Wheat starch dust with a k_c close to 0.86.

Furthermore, regarding to the estimation of $k_c = 0.86$ as a close value to the stoichiometric relation between dust mass and air into the combustion inside the 20L Sphere test, there were made several test to validate the behavior at different (F/A) and compared with the experimental data found by Dufaud, et al. [29].

Fig. 15 shows that the general behavior of the CFD results are in agreement with the experimental data reported by Dufaud, et al [29]. Nonetheless, the discrepancy between the starch dust data and CFD are significantly, confirming the predominance and rate-limiting step of pyrolysis during explosions of organic dust [29], [41]. Moreover, the CFD data had better agreement with the experimental data of pyrolysis gases combustion, because of the lack on the CFD simulations of the influence of solid particles on turbulence during dispersion stage and the absence of the interference of the solid particles on heat transfer upstream the flame front [29], [40], [61], [62].

Furthermore, the disagreement between CFD data and pyrolysis gases combustion was decreased as the (F/A) was decreased. This suggests that a better estimation of the k_c is a value slightly higher than 0.86. For that reason, it is necessary to set a more reliable model than the k_c to emulate the behavior of organic dust combustion on 20L Sphere test.

4. CONCLUSIONS

The CFD model constructed provides a fully accurate prediction of the sphere pressure given that the deviations from the experimental points (for the standard nozzle) do not overcome 8.6% for Wheat Starch and 5.5% for Carbon-black. Moreover, the initial agglomeration shape of Wheat starch does not have a considerable influence on the behavior of the sphere pressure with time. However, the geometrical differences between the nozzles and the turbulence levels reached in each case produce a variation of the pressure profile obtained.

The CFD model developed also leads to conclude that, during the dispersion step, the levels of turbulence undergo a significant decay at the first 20-30ms, followed by a less prominent decay up to the Ignition Delay Time that can be modelled by the inverse power-law relation proposed by Dahoe et al. [24]

On the other hand, the nozzle geometry modification marginally affects the de-agglomeration of Carbon-black particles on the sphere. However, the tendency is that the overriding stage of de-agglomeration is caused during the injection as the experimental and numerical results suggested, with a reduction of 68% and 45% of the mean diameter of Wheat starch and Carbon-black particles, respectively. This behavior is according to the high-pressure gradients when the particles moves through the canister exit to the nozzle, the baroclinic effect and the generation of rotary stresses. In addition, the PSD reduction with the cube configuration is closer to the experimental one than the obtained with the other shapes of Wheat starch. Therefore, this study suggested to use the Cube shape for future simulations that include agglomeration phenomena.

In addition, the real concentration is lower than the nominal concentration for all the different nozzle and agglomerates at the ignition time. For that reason, the MEC standard calculation has a significant disagreement. Nevertheless, the outlines of concentration ratio of carbon black with nozzle 6 develops a slightly better homogeneity, followed by nozzle, which can help to reduce the uncertainty in MEC determination.

Otherwise, the simulated combustion results show that the environment in which the pyrolysis gases are present at 60 ms is highly reactive, aided by the levels of turbulence that the system reaches. Moreover, the flame front is not perfectly spherical and, at certain times, has a preferred direction by the fact that there are still certain velocity gradients that direct the flame to a specific direction.

Additionally, the evaluation of $(dP/dt)_{max}$ of Wheat starch at different values of k_c have a significantly difference of one order of magnitude between the CFD and experimental data of combustion of the solid particles, validating the predominance and rate-limiting step of the pyrolysis during an organic dust explosion. Moreover, the use of a k_c to emulate the behavior of particles combustion is not practical, therefore it is necessary the study of the kinetics of the pyrolysis step of organic dust, as further work, to load to CFD software and generates a better fit to experimental data. Nevertheless, the CFD prediction has better agreement with the experimental data of pyrolysis gases combustion, because of the lack on the CFD simulations of the influence of solid particles on turbulence during dispersion stage and the absence of the interference of the solid particles on heat transfer upstream the flame front.

Finally, this study shows several uncertainties on assumptions and predictions of severity explosivity parameters on the 20L Sphere standard test, which affects the properly design of protection and safety devices. For that reason, it is suggested that a novel dust dispersion system should be considered to have more accurate and reliable results.

References

[1] A. Di Benedetto, P. Russo, R. Sanchirico, and V. Di Sarli, “CFD simulations of turbulent fluid flow and dust dispersion in the 20 liter explosion vessel,” *AIChE J.*, vol. 59, no. 7, pp. 2485–2496, Jul. 2013.

[2] J. Cross and D. Farrer, *Dust Explosions*, First. New York: Plenum Publishing, 1982.

[3] R. K. Eckhoff, *Dust Explosions in the Process Industries*. 2003.

[4] T. Abbasi and S. A. Abbasi, “Dust explosions-Cases, causes, consequences, and control,” *Journal of Hazardous Materials*, vol. 140, no. 1–2. pp. 7–44, 2007.

[5] P. R. Amyotte, “Some myths and realities about dust explosions,” *Process Saf. Environ. Prot.*, vol. 92, no. 4, pp. 292–299, 2014.

[6] P. R. Amyotte and R. K. Eckhoff, “Dust explosion causation, prevention and mitigation: An overview,” *J. Chem. Heal. Saf.*, vol. 17, no. 1, pp. 15–28, 2010.

[7] D. B. Mercer *et al.*, “The influence of injector design on the decay of pre-ignition turbulence in a spherical explosion chamber,” *J. Loss Prev. Process Ind.*, vol. 14, no. 4, pp. 269–282, 2001.

[8] R. K. Eckhoff, “Understanding dust explosions. The role of powder science and technology,” *J. Loss Prev. Process Ind.*, vol. 22, no. 1, pp. 105–116, 2009.

[9] A. Di Benedetto, P. Russo, P. Amyotte, and N. Marchand, “Modelling the effect of particle size on dust explosions,” *Chem. Eng. Sci.*, vol. 65, no. 2, pp. 772–779, 2010.

[10] A. Di Benedetto *et al.*, “Flame Propagation of Dust and Gas-Air Mixtures in a Tube,” *Chia Laguna, Cagliari, Sardinia*, vol. 1, pp. 11–13, 2011.

[11] G. Colonna, “Credible Risk,” *NFPA J.*, 2015.

[12] O. Kalejaiye, P. R. Amyotte, M. J. Pegg, and K. L. Cashdollar, “Effectiveness of dust dispersion in the 20-L Siwek chamber,” *J. Loss Prev. Process Ind.*, vol. 23, no. 1, pp. 46–59, 2010.

[13] ISO 6184-1, *Explosion protection systems. Part 1 : Determination of explosion indices of combustible dusts in air*, vol. 23, no. 1. 1985.

[14] ASTM, “ASTM E1226-12a Standard Test Method for Explosibility of Dust Clouds,” *ASTM Int.*, pp. 1–13, 2012.

[15] ASTM, “ASTM E2019 - 03 Standard Test Method for Minimum Ignition Energy of a Dust Cloud in Air,” *ASTM Int.*, pp. 1–13, 2003.

[16] A. G. Dastidar, “ASTM E2931: A new standard for the limiting oxygen concentration of combustible dusts,” *Process Saf. Prog.*, vol. 35, no. 2, pp. 159–164, 2016.

[17] ASTM, “ASTM E1515-14: Standard Test Method for Minimum Explosible Concentration of Combustible Dusts,” *ASTM Int.*, pp. 1–9, 2014.

[18] ASTM, “ASTM E1491 - 06(2012) Standard Test Method for Minimum Autoignition Temperature of Dust Clouds,” *ASTM Int.*, pp. 1–12, 2012.

[19] R. Sanchirico, V. Di Sarli, P. Russo, and A. Di Benedetto, “Effect of the nozzle type on the integrity of dust particles in standard explosion tests,” *Powder Technol.*, vol. 279, pp. 203–208, 2015.

[20] D. Vizcaya *et al.*, “CFD as an approach to understand flammable dust 20 L standard test: Effect of the ignition time on the fluid flow,” *AIChE J.*, vol. 64, no. 1, pp. 42–54, Jan. 2018.

[21] J. Yuan, W. Huang, H. Ji, N. Kuai, and Y. Wu, “Experimental investigation of dust MEC measurement,” *Powder Technol.*, vol. 217, pp. 245–251, 2012.

[22] Q. Zhang and B. Zhang, “Effect of ignition delay on explosion parameters of corn dust/air inconfined chamber,” *J. Loss Prev. Process Ind.*, vol. 33, pp. 23–28, 2015.

[23] A. E. Dahoe *et al.*, “Dust Explosions in Spherical Vessels : prediction of the pressure evolution and determination of the burning velocity and flame thickness,” *Proc. 7th Int. Colloq. Dust Explos.*, pp. 67–87, 1996.

[24] A. E. Dahoe, R. S. Cant, and B. Scarlett, “On the decay of turbulence in the 20-liter explosion sphere,” *Flow, Turbul. Combust.*, vol. 67, no. 3, pp. 159–184, 2002.

[25] A. E. Dahoe, R. S. Cant, M. . Pegg, and B. Scarlett, “On the transient flow in the 20-liter explosion sphere,” *J. Loss Prev. Process Ind.*, vol. 14, no. 6, pp. 475–487, 2001.

[26] B. Du *et al.*, “Visualization and analysis of dispersion process of combustible dust in a transparent Siwek 20-L chamber,” *J. Loss Prev. Process Ind.*, vol. 33, pp. 213–221, 2015.

[27] C. Murillo *et al.*, “Proposal of a new injection nozzle to improve the experimental reproducibility of dust explosion tests,” *Powder Technol.*, vol. 328, pp. 54–74, 2018.

[28] C. Murillo, “Experimental and numerical approaches to particles dispersion in a turbulent flow: application to dust explosions,” Université de Lorraine, 2016.

[29] O. Dufaud *et al.*, “Comparing pyrolysis gases and dusts explosivities: A clue to understanding hybrid mixtures explosions?,” *Industrial and Engineering Chemistry Research*, vol. 51, no. 22. pp. 7656–7662, 2012.

[30] N. Cuervo, “Influences of turbulence and combustion regimes on explosions of gas-dust hydrid mixtures,” University of Lorraine, 2015.

[31] P. G. J. van der Wel, J. P. W. van Veen, S. M. Lemkowitz, B. Scarlett, and C. J. M. van Wingerden, “An interpretation of dust explosion phenomena on the basis of time scales,” *Powder Technol.*, vol. 71, no. 2, pp. 207–215, 1992.

[32] S. Callé, L. Klaba, D. Thomas, L. Perrin, and O. Dufaud, “Influence of the size distribution and concentration on wood dust explosion: Experiments and reaction modelling,” in *Powder Technology*, 2005, vol. 157, no. 1–3, pp. 144–148.

[33] K. L. Cashdollar, “Coal dust explosibility,” *J. Loss Prev. Process Ind.*, vol. 9, no. 1 SPEC. ISS., pp. 65–76, 1996.

[34] R. Soundararajan, P. R. Amyotte, and M. J. Pegg, “Explosibility hazard of iron sulphide dusts as a function of particle size,” *J. Hazard. Mater.*, vol. 51, no. 1–3, pp. 225–239, 1996.

[35] R. K. Eckhoff, “Does the dust explosion risk increase when moving from μm-particle powders to powders of nm-particles?,” *J. Loss Prev. Process Ind.*, vol. 25, no. 3, pp. 448–459, 2012.

[36] T. Skjold, B. J. Arntzen, O. R. Hansen, I. E. Storvik, and R. K. Eckhoff, “Simulation of dust explosions in complex geometries with experimental input from standardized tests,” in *Journal of Loss Prevention in the Process Industries*, 2006, vol. 19, no. 2–3, pp. 210–217.

[37] Z. Salamonowicz, M. Kotowski, M. Półka, and W. Barnat, “Numerical simulation of dust explosion in the spherical 20l vessel,” *Bull. Polish Acad. Sci. Tech. Sci.*, vol. 63, no. 1, pp. 289–293, 2015.

[38] R. Redlinger, “Numerical simulation of hybrid dust/gas explosion experiments in the standard 20-L sphere,” *Fusion Eng. Des.*, vol. 100, pp. 419–424, 2015.

[39] A. K. Prasad, “Particle image

velocimetry," *Curr. Sci.*, vol. 79, no. 1, pp. 51–60, 2000.

[40] D. Torrado, N. Cuervo, S. Pacault, P. A. Glaude, and O. Dufaud, "Influence of carbon black nanoparticles on the front flame velocity of methane/air explosions," *J. Loss Prev. Process Ind.*, vol. 49, pp. 919–928, 2017.

[41] N. Cuervo, O. Dufaud, D. Torrado, N. Bardin-monnier, L. Perrin, and A. Laurent, "Experimental Study and Modelling of the Pyrolysis of Organic Dusts : Application to Dust Explosions," vol. 31, pp. 931–936, 2013.

[42] O. Bozier, "Contribution à l'étude des caractéristiques de combustion isochores d'une suspension de particules solides réactives. Génération de la suspension, influence de l'état initial du mélange," Universitè de Poitiers, 2004.

[43] H. Zhang *et al.*, "Effects of particle size on flame structures through corn starch dust explosions," *J. Loss Prev. Process Ind.*, vol. 50, pp. 7–14, 2017.

[44] T. Lu and C. K. Law, "A criterion based on computational singular perturbation for the identification of quasi steady state species: A reduced mechanism for methane oxidation with NO chemistry," *Combust. Flame*, vol. 154, no. 4, pp. 761–774, Sep. 2008.

[45] Siemens PLM, "STAR-CCM+ Simcenter Documentation," 2018. [Online]. Available: https://documentation.thesteveportal.plm.automation.siemens.com/starccmplus_latest_en/index.html?param=XxShn&authLoc=https://thesteveportal.plm.automation.siemens.com/AuthoriseRedirect.

[46] C. Murillo, N. Bardin-monnier, C. Blanchard, F. Munoz, N. Ratkovich, and D. Vizcaya, "CFD to Improve the Repeatability and Accuracy of Dust Explosion Tests in the 20-liters Sphere," *Chem. Eng. Sci.*, vol. 48, no. January, pp. 115–120, 2016.

[47] D. C. Wilcox, *Turbulence modeling for CFD*. 1993.

[48] S. R. Shah, S. V. Jain, R. N. Patel, and V. J. Lakhera, "CFD for centrifugal pumps: A review of the state-of-the-art," *Procedia Eng.*, vol. 51, no. NUiCONE 2012, pp. 715–720, 2013.

[49] C. Murillo, N. Bardin-Monnier, F. Muñoz, and O. Dufaud, "Application of CFD on the sensitivity analyses of some parameters of the modified Hartmann tube," *J. Loss Prev. Process Ind.*, vol. 36, pp. 296–307, 2015.

[50] H. Zhou, K. Cen, and J. Fan, "Detached eddy simulation of particle dispersion in a gas-solid two-phase fuel rich/lean burner flow," *Fuel*, vol. 84, no. 6, pp. 723–731, 2005.

[51] M. Wang, C. H. Lin, and Q. Chen, "Advanced turbulence models for predicting particle transport in enclosed environments," *Build. Environ.*, 2012.

[52] R. Ben Moussa, M. Guessasma, C. Proust, K. Saleh, and J. Fortin, "Thermal radiation contribution to metal dust explosions," in *Procedia Engineering*, 2015, vol. 102, pp. 714–721.

[53] H. Yu, W. Cheng, L. Wu, H. Wang, and Y. Xie, "Mechanisms of dust diffuse pollution under forced-exhaust ventilation in fully-mechanized excavation faces by CFD-DEM," *Powder Technol.*, vol. 317, pp. 31–47, 2017.

[54] A. Di Renzo and F. P. Di Maio, "Comparison of contact-force models for the simulation of collisions in DEM-based granular flow codes," *Chem. Eng. Sci.*, vol. 59, no. 3, pp. 525–541, 2004.

[55] D. Torrado, "Effect of carbon black nanoparticles on the explosion severity of gas mixtures," Université de Lorraine, 2017.

[56] M. Amin, "EXPERIMENTAL AND COMPUTATIONAL ASSESSMENT OF THE STANDARD TEST FOR

DUST CHARACTERIZATION BASED ON THE DEGREE OF AGGLOMERATION AND DE-AGGLOMERATION," Universidad de los Andes, 2017.

[57] A. Pinilla, "CFD study on the incidence of the change of nozzle on the dust dispersion in the 20 liters sphere.," Universidad de los Andes, 2017.

[58] P. Orlandi and J. Jiménez, "On the generation of turbulent wall friction," *Phys. Fluids*, vol. 6, no. 2, pp. 634–641, 1994.

[59] C. Weiler, M. Wolkenhauer, M. Trunk, and P. Langguth, "New model describing the total dispersion of dry powder agglomerates," *Powder Technol.*, vol. 203, no. 2, pp. 248–253, Nov. 2010.

[60] L. A. Turkevich, A. G. Dastidar, Z. Hachmeister, and M. Lim, "Potential explosion hazard of carbonaceous nanoparticles: Explosion parameters of selected materials," *J. Hazard. Mater.*, vol. 295, pp. 97–103, 2015.

[61] D. Torrado *et al.*, "Numerical study of the influence of particle reaction and radiative heat transfer on the flame velocity of gas/nanoparticles hybrid mixtures," *Process Saf. Environ. Prot.*, vol. 118, pp. 211–226, 2018.

[62] D. Torrado, P. Glaude, and O. Dufaud, "Effect of carbon black nanoparticles on methane/air explosions: Influence at low initial turbulence," *J. Phys. Conf. Ser.*, vol. 838, p. 012022, Jun. 2017.